



Simulation of machining behaviour of two-phase brittle materials during grinding by modelling single-grain scratching using a combination of FE and SPH methods

Alexander Dehmer¹ · Sebastian Prinz¹ · Peter Breuer¹ · Sebastian Barth¹ · Thomas Bergs²

Received: 15 February 2023 / Accepted: 17 July 2023 / Published online: 28 July 2023
© The Author(s) 2023

Abstract

Two-phase, brittle-hard materials are widely used not only in the tool industry but also increasingly in the aerospace industry. Due to the two-phase nature, the materials have unique material properties adapted to the respective application. But the material properties also lead to challenging machinability. Therefore, two-phase, brittle-hard materials are mostly ground. The analogy process of single-grain scratching is used to analyse the material removal behaviour and design the grinding process. Since single-grain scratching is time-consuming and costly, it is desirable to substitute the analogy process with numerical simulation. This paper discusses the suitability of the Smooth Particle Hydrodynamic (SPH) simulation method in combination with the Finite Element Method (FEM) for single-grain scratching of two-phase, brittle-hard materials. The approach is validated using the examples of tungsten carbide-cobalt (WC-Co) cemented carbides and Silicon carbide fibre-reinforced silicon carbide (SiC/SiC) ceramics. For both applications, the material removal behaviour was optically analysed and in good agreement with the experimental results and theoretical assumptions. For SiC/SiC ceramics, several surface phenomena could be identified in the simulation as well as in the experimental results. The scratching forces were compared qualitatively and were in good agreement with the experimental results for both applications.

Keywords Grinding technology · Brittle materials · SPH · FEM · Single-grain scratching · Numerical simulation

1 Introduction

Two-phase, brittle materials are used in a wide variety of industries. For example, tungsten carbide-cobalt (WC-Co) cemented carbides have been used as cutting materials in tool manufacturing [1]. A new development uses Silicon carbide fibre-reinforced silicon carbide (SiC/SiC) ceramics in the aerospace industry [2]. Both WC-Co cemented carbides and SiC/SiC ceramics are classified as brittle materials due to their material properties, a combination of the properties of the individual phases [3]. In both applications, high accuracies with high productivity are required [4].

Due to the challenging material properties of the two-phase, brittle materials for machining, only grinding achieves the necessary high productivity and high accuracy [5]. Because of the complex and indeterminate cutting-edge geometries and many simultaneous grain engagements, the material removal behaviour cannot be analysed in the grinding process. Therefore, the material removal behaviour is usually investigated with the analogy process of single-grain scratching [6]. Novel approaches go as far as working with cutting speeds of up to 40.2 m/s [7] whilst having a nano-scale depth of cut in order to be able to reproduce special grinding processes, such as ultra-precision grinding [8]. Next to the material removal behaviour during grinding, these approaches also enable the tracking of microcrack propagation [9]. However, single-grain scratching investigations are time-consuming and costly and must be carried out for a wide variety of material specifications, grain geometries, and process parameters.

One possibility to substitute single-grain scratching investigations is numerical simulation [10]. In addition to cost and time savings, a numerical simulation can contribute to

✉ Alexander Dehmer
alexander.dehmer@rwth-aachen.de

¹ Laboratory for Machine Tools and Production Engineering WZL, RWTH Aachen University, Campus-Boulevard 30, D-52074 Aachen, Germany

² Fraunhofer Institute for Production Technology IPT, Steinbachstraße 17, 52074 Aachen, Germany

an improved understanding of the material removal process in grinding since experimental investigations only allow a limited insight into the contact zone between the workpiece and tool due to the complex engagement conditions. With that knowledge gained, the grinding process design will be more efficient [11].

This work used the Smooth Particle Hydrodynamics (SPH) method to simulate the single-grain scratching of WC-Co cemented carbide and SiC/SiC ceramics as examples of two-phase brittle materials. The simulations were validated with experimental data.

2 Simulation of brittle materials using SPH

The SPH method is a calculation method for the realisation of manufacturing simulations. It was developed by Lucy [12] and by Gingold and Monaghan [13] to simulate astrophysical problems. Later, it was used for solid mechanics investigations [14].

When the SPH method is applied, the continuum is approximated by a finite number of uncrosslinked particles. Each particle is assumed to have its properties at the centre of mass. These properties are determined using interpolation from the corresponding properties of the surrounding particles. The interpolation is described by the smoothing function W . Figure 1 illustrates the smoothing function and its sphere of influence on surrounding elements.

W depends on the smoothing length h and the distance ($r_i - r_j$) of a considered particle from the surrounding particles. r_i and r_j describe the position of the individual particles in the selected coordinate system. Therefore, W is defined according to formula (1) [15]:

$$W = W(r_i - r_j, h) \quad (1)$$

The selection of the smoothing function used for a simulation depends on the particular application. The following criteria must be considered: the function must be positive

and radially symmetric around r_i . In the range of validity, which is a circle with the radius h around r_i , the integral must be 1 (normalisation). Outside the range of validity, the function value must be 0. When approaching r_i , W must behave according to a delta function. In other words, the function value must fall monotonically with increasing distance from r_i [15]. The term delta function denotes a function with a value of 0 at every point except 0, whilst its infinite integral has the value 1 [16]. Seventeen parameters describe the properties of SPH particles. These include the position, the velocity in all directions, the density, the internal energy, the mass, and the damage. Thus, formula (2) applies to each of the quantities A , which have to be calculated [17]:

$$A(r_i) = \int A(r_j) \cdot W(r_i - r_j, h) dr' \quad (2)$$

Formula (2) shows that the smoothing function W decreases with increasing distance from the considered particle ($r_i - r_j$). Thus, on the calculated properties of the considered particle, the properties of more distant particles within the smoothing length have a smaller influence than closer particles. The limits of the interpolation are defined by the smoothing length h [15].

Assigning properties to points that do not coincide with the centre of mass of an SPH particle can be done in several ways. Lucy [12], as well as Gingold and Monaghan [13], used a statistical method. Alternatively, the actual particle density of the neighbouring particles can be considered in the interpolation, as in the simulation software LS-Dyna of the company Livermore Software Technology Corporation. In this case, the calculation is performed according to formula (3). Here, the parameter J denotes the number of particles involved, m_j the mass of particle j , and ρ_j its density [18].

$$A(r_i) = \sum_{j=1}^J \frac{m_j}{\rho_j} A(r_j) \cdot W(r_i - r_j, h) \quad (3)$$

The SPH method was originally developed to describe fluids. However, the calculation does not distinguish between particles of different aggregate states [17]. Thus, adapted material models are used to adequately represent the force transfer behaviour of solids [18].

An advantage of the SPH method concerning the stability and efficiency of machining simulations is that, regardless of the magnitude of deformations and deformation velocities, no mesh and, therefore, no remeshing is required [19]. Thus, for large deformations and deformation velocities, shorter computation times can be achieved than, for example, in a finite element (FE) simulation [20].

It is possible to combine the FE and SPH methods. Combined simulations can achieve shorter computation times than pure SPH simulations whilst maintaining high accuracy by using finite elements for the non-deformed or only slightly

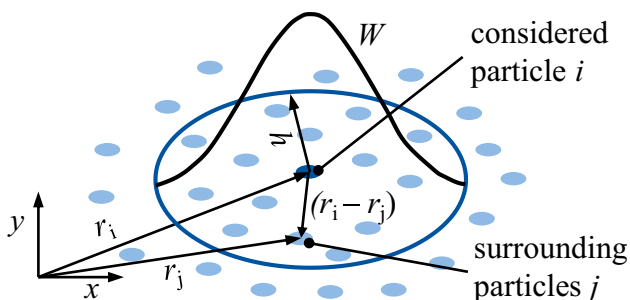


Fig. 1 Smoothing function and its sphere of influence according to Fraga Filho [15]

deformed tool and SPH particles for the workpiece [21]. Another possible combination of the FE and SPH methods is the representation of workpiece regions far away from the workpiece-tool contact by finite elements [22].

Using the FE method to simulate brittle materials, different criteria must be defined to ensure the mesh is free of gaps and overlaps. Defining criteria is not necessary using the SPH method [23]. The propagation of a crack in a workpiece modelled with SPH particles is inherently due to the change in particle spacing. Therefore, the calculated stress state is not distorted by the deletion of overloaded elements, as in the FE method [24]. The SPH method allows a high calculation accuracy, especially for the simulation of cutting processes with negative rake angles, like grinding [25].

Using the SPH method, adapted material models are required to map the force transfer behaviour in solids [18]. Examples are the viscoplastic material models Johnson-Holmquist 2 (JH2) and Johnson-Cook (JC). The JH2 model includes a strength model, a damage model, and a volume-pressure model. The calculated strength values depend on the pressure p , the strain rate $\dot{\epsilon}$, and the damage variable D . The damage variable D is included in the further calculations in the JH2 model by interpolation between a calculation rule for a completely intact material ($D = 0$) and a wholly damaged material ($D = 1$) [26].

The SPH method was already used for simulations of brittle materials. Niu et al. [27] used the SPH method to simulate the machining process of an aluminium alloy. They achieved more accurate chip morphology predictions than a FE simulation but required longer computation times. Less simplifying assumptions were required for chip formation and meshing than in FE simulation. Wang et al. [28] used a combined FE-SPH simulation to study an ultrasonic-assisted glass machining process. Finite elements represented the tool, and SPH particles represented the workpiece. The results could be validated experimentally. Abena and Essa [29] compared the FE and SPH methods for simulating the machining of carbon fibre-reinforced plastics. The chip geometry determined by the SPH method showed a more accurate agreement with the chip geometry in the actual process. For a large part of the investigated fibre orientations, the process forces were also predicted more accurately than with the FE method. Deng et al. simulated a milling process of zircon ceramics using a combined FE-SPH approach. They determined critical chip thicknesses and chip shapes depending on the rake angle of the tool and other process parameters [21]. Sridhar and Parebruyne [30] performed a comparative study of FE and SPH simulation for

a turning process of aluminium. All investigated approaches allowed an accurate prediction of the experimentally determined chip geometries. The process forces calculated using the SPH method showed a minor deviation from the experimental values.

3 Modelling the single-grain scratching process

The following describes the models for simulating single-grain scratching of both WC-Co cemented carbide and SiC/SiC ceramics. Since the mesostructure of the materials differs a lot, the models vary significantly as well. Therefore, the WC-Co cemented carbide and SiC/SiC ceramics models are discussed separately. The software LS-Dyna from Livermore Software Technology Corporation was used for both models.

3.1 WC-Co cemented carbide

WC-Co cemented carbides are two-phase materials used, for example, to manufacture cutting tools. The basis for this application is that cemented carbides combine a high hardness with a high fracture toughness. However, these properties also result in difficult machinability. Therefore, WC-Co cemented carbides are mostly ground. WC-Co cemented carbides are classified into specifications. These are characterised by a mean WC grain diameter d_{WC} and a Co fraction x_{Co} . The material removal behaviour of the cemented carbides depends on the specification. Currently, process design in grinding is mostly done by preliminary tests. An alternative to avoid time- and cost-intensive initial tests is simulation.

The simulation of the single-grain scratching process of WC-Co cemented carbide focused on determining the occurring scratching forces as a function of the WC-Co cemented carbide specification and the scratching process parameters. The selected cemented carbide specifications by Ceratizit SA and the simulated process parameters were derived from scratching tests already performed, which could be used for validation (see also Section 4.1.1). The cemented carbide specifications are shown in Table 1. A cutting speed of $v_c = 20$ m/s was used for both the numerical and the empirical tests.

In this work, single-grain scratching was investigated as an analogy process to the grinding process. During

Table 1 Cemented carbide specifications used in this work

Variation of cemented carbide	CTF08E	CTF12E	CTF24E	CTF40A	CTS12L
Co fraction x_{Co} (%)	4	6	12	20	6
Mean WC grain diameter d_{WC} (μm)	0.8–1.3	0.8–1.3	0.8–1.3	0.8–1.3	0.5–0.8

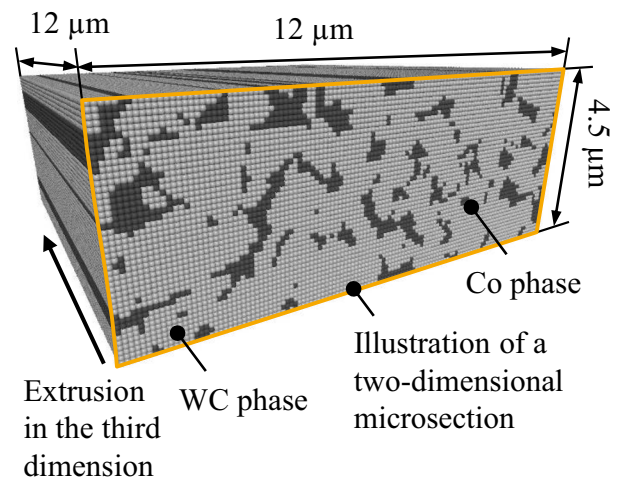
Table 2 Material parameters of WC and Co according to Kurlov et al. [32], Csanádi et al. [33], Özden [34], and Kurzweil [35]

	WC	Co
Material model	Linear elastic ideal plastic	Linear elastic linear plastic
Density ρ (kg/cm ³)	0.0157	0.00889
Shear modulus G (MPa)	274,000	87,415
Yield stress σ_y (MPa)	6450	683.07
Tangent modulus E_T (MPa)	0	1783
Compressive modulus K (MPa)	629,700	189,400

grinding, strain rates $\dot{\epsilon} > 10^6 \text{ s}^{-1}$ may be present on the workpiece [31]. The SPH method is more efficient in simulating high strain rates and was therefore chosen for modelling the workpiece. The respective material behaviour of the WC and the Co phases was approximated in the mesoscopic simulation by a linear elastic-ideal plastic (WC) and a linear elastic-linear plastic material model (Co). The used material parameters were derived from the literature and are shown in Table 2.

LS-Dyna allows two- and three-dimensional simulations to be performed. A complex, three-dimensional geometry characterised the diamond grains studied in this work. In addition, the cemented carbide workpieces exhibited a three-dimensional mesogeometry. Consequently, the representation of the single-grain scratching process in three dimensions is required for realistic modelling. However, information on the cemented carbide mesogeometry was only available in two-dimensional scanning electron micrographs of microstructural sections. The two-dimensional image was linearly extruded into the remaining third spatial direction by transferring the scanning electron micrographs into the third dimension (Fig. 2). The chosen approach thus allows the spatial mapping of the considered process in terms of diamond grain geometry and displacement of material particles from their original position, without presupposing information on the three-dimensional mesogeometry of the material in its initial state.

During the simulation model's development, a central challenge was to identify a suitable compromise between a high level of detail compared to the actual process and a moderate calculation time. A key parameter influencing the calculation time was the particle spacing a_p . The largest possible particle spacing a_p with sufficient accuracy of the computation result was selected to minimise the computation time. Another requirement was to choose an equal value of the particle spacing a_p for different cemented carbide specifications to ensure the comparability of the simulation results. Based on a visual comparison of the generated material mesogeometry models with the underlying micrographs of all cemented carbide specifications,



Cemented carbide CTF24E	Co fraction x_{Co} 12 %
Mean WC grain diameter d_{WC} 0.8–1.3 μm	

Fig. 2 Exemplary three-dimensional cemented carbide mesogeometry model for CTF24E

a particle spacing $a_p = 0.1 \mu\text{m}$ was identified as suitable, which resulted in a total number of SPH particles $n_p = 756,000$.

To further reduce the model complexity, the size of the section of the mesostructure was chosen so that only workpiece areas influenced by the single-grain scratching process were included in the simulation. The length, width, and height of this segment and the infeed of the diamond grain were determined iteratively. In this manner, an infeed of $a_{e,num} = 1.5 \mu\text{m}$ was determined even though the infeed of the experiments $a_{e,emp} = 20 \mu\text{m}$ was much higher. The width of the considered workpiece section was $b_w = 12 \mu\text{m}$ in all simulations, and the height in the infeed direction was $h_w = 4.5 \mu\text{m}$. The length of the workpiece in the scratching direction was determined to be $l_w = 12 \mu\text{m}$ for the cemented carbide specifications CTF08E, CTF12E, CTF24E, and CTS12L. For the cemented carbide specification CTF40A, a greater length of $l_{w,CTF40A} = 14 \mu\text{m}$ was required because the effects of the rear workpiece edge plane on the simulation were apparent earlier.

The diamond grains meshed with FE were assumed to be non-deformable and were modelled using 3D laser scanning microscope (LSM) images of grains. The procedure to derive a meshed grain geometry integrated into the simulation is illustrated in Fig. 3.

Based on the simulation of individual grain engagements, it was possible to model the diamond grain as rigid. This approach is comparable to the method of Umer et al. [19]

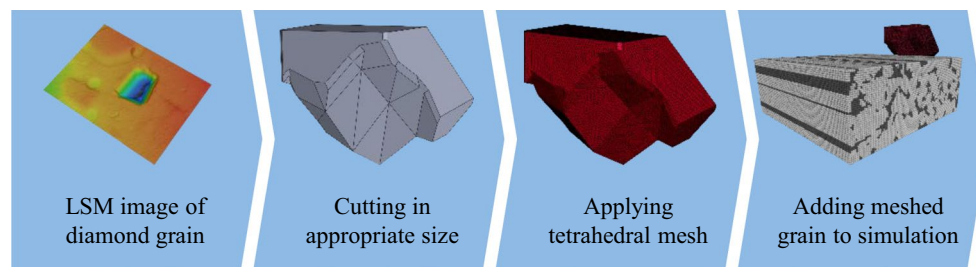


Fig. 3 Integrating a real diamond grain geometry in the simulation meshed with FE

Table 3 Material parameters of diamond for a rigid body material model [36]

	Density ρ (kg/cm ³)	Young's modulus E (MPa)	Poisson's ratio ν (-)
Diamond	0.00352	890,000	0.2

and is based on the assumption that wear on the diamond grain only occurs after repeated grain engagements. The diamond grain was modelled with finite elements since FE simulations calculate rigid bodies more efficiently. The mesh size of the tetrahedral mesh was chosen to be $\Delta_{\text{mesh}} = 0.1 \mu\text{m}$ according to the particle distance of the SPH-modelled workpiece. Due to the complex diamond grain geometry and the small mesh size, other FE geometries were ruled out. The material properties of diamonds needed to model a rigid body are shown in Table 3.

In addition to the geometric and physical modelling, boundary and contact conditions must be defined. As shown in Fig. 4, the particles of the two sidewalls (blue) and the particles at the lower model edge (yellow) were fixed in all translational and rotational degrees of freedom. The boundary condition described was chosen because the fixed degrees of freedom in these locations had little effect on the simulated material behaviour on the sides where the diamond grain enters and exits and on the machined surface of the workpiece. The fixed degrees of freedom represented the embedding of the workpiece in the surrounding material as well as its fixation in a test arrangement.

The rotational movement of the diamond grain in the real scratching process can be assumed to be negligible in the context of the simulation due to the small amount of infeed. The motion of the diamond grain in the simulation was therefore modelled as uniaxial translational motion.

Because both phases were modelled with SPH particles and due to the structure of a SPH simulation, no contact conditions had to be modelled between Co and WC. Within the SPH simulation, the interaction between both phases is calculated automatically. A contact model had to be determined between the two-phase workpiece and the diamond

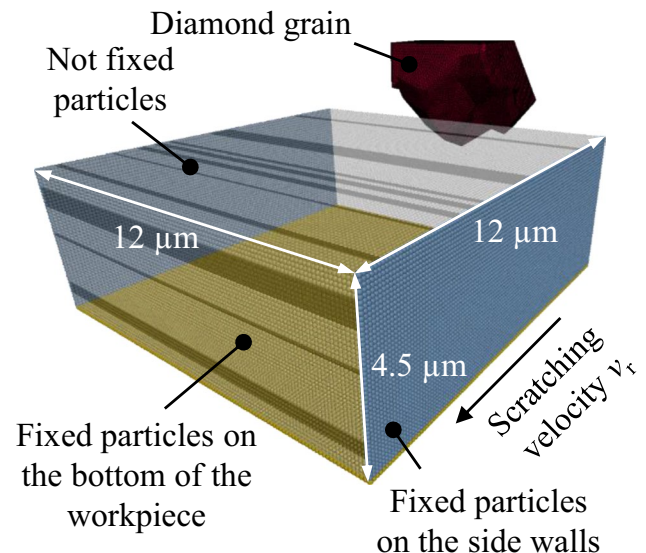


Fig. 4 Fixed boundary conditions of the workpiece

grain, which was discretized by finite elements. For this purpose, the static friction coefficient μ_s and the dynamic friction coefficient μ_d between the workpiece and the diamond grain were defined. No literature values were available for the friction coefficients. Therefore, they were approximated by values determined by Jianxin et al. in tribological investigations for a WC-Co cemented carbide in contact with aluminium oxide Al_2O_3 [37]. The static friction coefficient was determined to be $\mu_s = 0.35$, and the dynamic friction coefficient to be $\mu_d = 0.2$. The parameters used for the simulation when single-grain scratching WC-Co cemented carbides are summarised in Table 4.

3.2 SiC/SiC ceramics

SiC/SiC is a new generation of high-temperature lightweight ceramic matrix composite material. SiC/SiC has higher specific strength than titanium and nickel-based superalloys above 1000°C as well as good high-temperature fracture toughness, creep, and other material properties

Table 4 Parameters used for simulating single-grain scratching of WC-Co cemented carbides

Parameter	Description	Value	Unit
$a_{e,num}$	Simulation infeed	1.5	μm
a_p	SPH particle spacing of workpiece	0.1	μm
b_w	Workpiece width	12	μm
h_w	Workpiece height	4.5	μm
l_w	Workpiece length for other WC-Co specifications	12	μm
$l_{w,CTF40A}$	Workpiece length for CTF40A	14	μm
n_p	Number of SPH particles	756,000	-
v_c	Cutting speed	20	m/s
Δmesh	FE mesh size of diamond grain	0.1	μm
μ_d	Dynamic friction coefficient	0.2	-
μ_s	Static friction coefficient	0.35	-

for the blade, vane, combustor, and shroud applications in critical hot sections of aircraft and power generation turbines [38]. Furthermore, SiC/SiC is one-third of the weight of traditional nickel-based superalloys. The reduced weight and elevated combustion temperature increase the efficiency and thrust of turbines [39, 40].

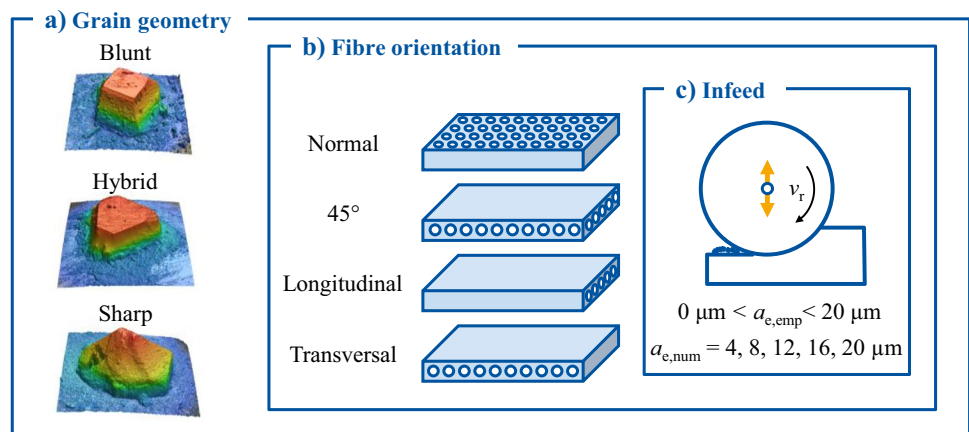
SiC/SiC comprises SiC fibre bundles (10–20 μm in diameter) embedded in the SiC ceramic matrix [41]. The fibre-reinforced microstructure of SiC/SiC overcomes the inherent limitation on the toughness of monolithic SiC ceramic. To further improve the toughness of SiC/SiC, the fibre-matrix was connected with a thin (about 1 μm) pyrolytic carbon (PyC) or boron nitride (BN) coating as the fibre-matrix interfacial material [42].

In the simulation, the material removal behaviour of the SiC/SiC ceramic during single-grain engagement with a diamond grain is numerically modelled. The results of the simulation were validated qualitatively and quantitatively with the results of previously conducted empirical single-grain scratching tests (see also Section 4.2.1).

Comparable to the simulation of the WC-Co cemented carbides, the wear of the diamond grain is negligible due to the short engagement time. Therefore, the diamond grain was assumed to be rigid and modelled with FE. The selected material parameters for the diamond corresponded to those used in the WC-Co cemented carbide model. Due to the high deformations during machining, the SPH method was selected to model the SiC/SiC ceramic. Likewise, cracks occurring as a result of brittle-hard machining can be better represented by the SPH method [43].

Based on the validation of the numerical simulation with the help of existing empirical test results, the process parameters of the simulation varied according to the conducted tests. In the empirical and numerical tests, the influence of three grain geometries—blunt, hybrid, and sharp—on the scratching of the fibre-reinforced SiC/SiC ceramics was investigated (Fig. 5a). For each grain geometry, the influence of the fibre orientation on the machining was investigated. For this purpose, the SiC/SiC samples were scratched in transverse, longitudinal, 45° and normal orientation (Fig. 5b). Caused by the selected scratching kinematics, the infeed varied between $0 < a_{e,emp} < 20 \mu\text{m}$ for each scratching track. Since this kinematics could not be reproduced in LS-Dyna, the discrete infeed $a_{e,num} = 4, 8, 12, 16, 20 \mu\text{m}$ were chosen for the numerical simulation (Fig. 5c). The cutting speed was set to $v_c = 20 \text{ m/s}$ for all simulations.

Calculation capacities of the High-Performance Cluster of RWTH Aachen University were used to run the simulations. There was a limitation of 24 hours for each simulation using the CPU with 16 cores and 1 GB memory for each core as well as a frequency of 2.1 GHz. In preliminary numerical tests, it was found that the calculation time strongly depends on the number of particles in the workpiece model. The workpiece dimensions had to be limited to achieve realistic calculation times of less than 24 hours per simulation. Therefore, it was impossible to represent

Fig. 5 Parameters variation of numerical and empirical single-grain scratching tests of SiC/SiC

the complete process kinematics of single-grain scratching in one simulation. A distinction had to be made between a model used to predict forces and a model used to predict the surface. Figure 6 shows the general difference in the

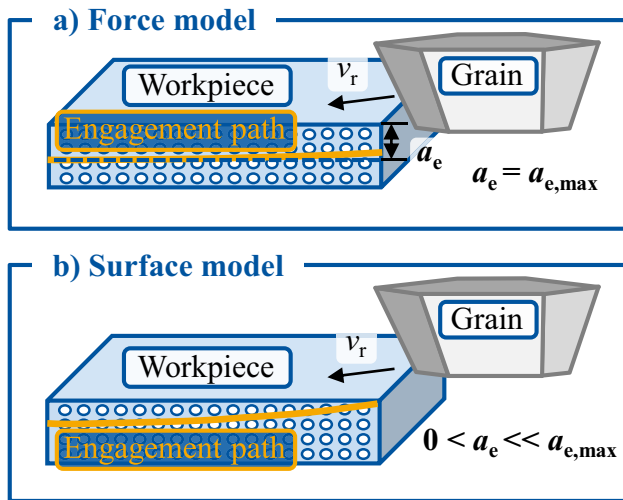
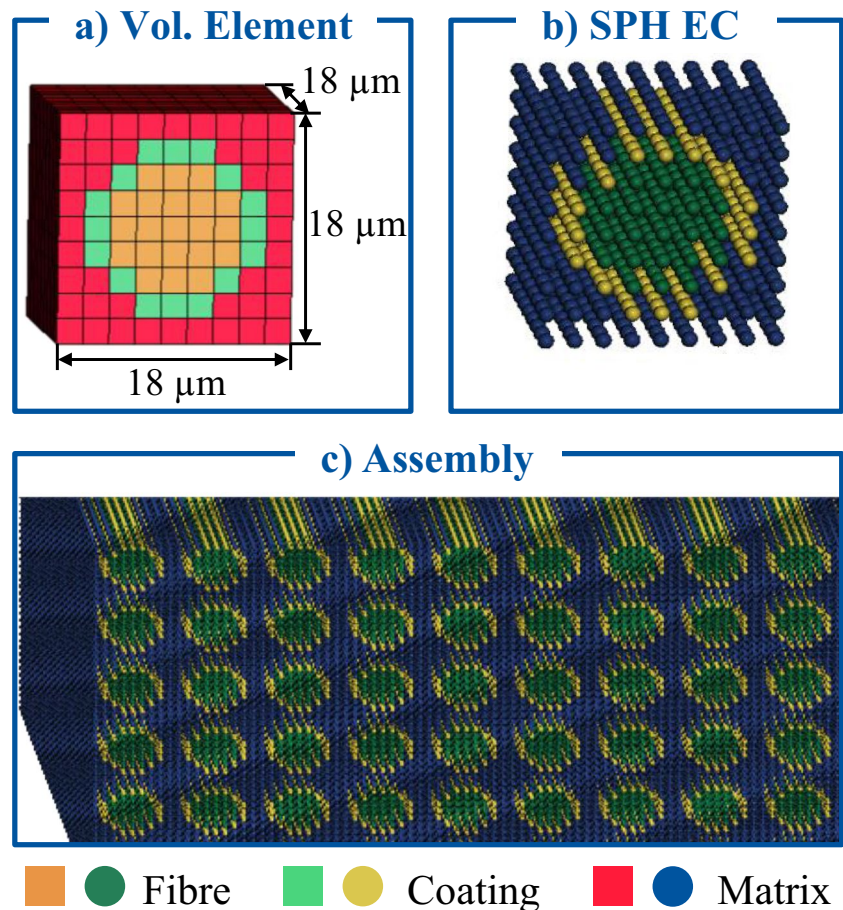


Fig. 6 Numerical models for force and workpiece surface

underlying process kinematics. In the force model, the material removal of the SiC/SiC ceramic already started with a predefined infeed a_e (Fig. 6a). The objective of the force model was to capture the maximum process forces during machining. On the other hand, in the surface model, the diamond grain was positioned in front of the workpiece without a preliminary infeed a_e (Fig. 6b). The objective of the second model was to capture the material removal mechanisms during the initial engagement of the diamond grain with the workpiece.

According to the data on the material used in the empirical tests, the SiC/SiC ceramic was modelled with SPH particles, for which a particle spacing $a_p = 2 \mu\text{m}$ was specified. Starting from a volume element (Fig. 7a), an elementary cell (EC) with the particle number $n_{p,EC} = 729$ was derived (Fig. 7b). The individual ECs were then assembled to form the final geometry of the SiC/SiC ceramic workpiece (Fig. 7c). For the force model, the length was modelled with 16, the width was modelled with 16, and the height was modelled with 6 ECs. The final sample dimensions resulted in $0.288 \times 0.288 \times 0.108 \text{ mm}^3$ and a total particle number of $n_{p,fm} = 1,119,744$. For the surface model, the length was modelled with 20, the width was modelled with 14, and the

Fig. 7 SPH modelling of the SiC/SiC ceramic



height was modelled with 5 ECs. The modelled sample had the final dimensions $0.36 \times 0.252 \times 0.09 \text{ mm}^3$ and a total particle number of $n_{p,sm} = 1,020,600$.

The challenge of numerically modelling the brittle material behaviour of the silicon carbide matrix was solved by using the JH2 material model [26]. Known as the most widely used material model to represent the post-fracture behaviour of ceramics, the JH2 model includes the main damage components of ceramics. The effects of ongoing damage are represented by a damage variable D . A disadvantage of the JH2 model is the high number of empirically determined material parameters required. For the SiC/SiC ceramic, these parameters were derived from an already validated model [44].

Due to the limited availability of the required material parameters of the Tyranno S fibre and the pyrolytic carbon fibre coating, a linear elastic ideal plastic material behaviour was assumed. The material parameters derived from the material manufacturers BJS Composites GmbH, UBE Industries Ltd., and the literature are listed in Table 5.

Table 5 Material parameters of the SiC fibre and the pyrolytic carbon coating for linear elastic ideal plastic material models according to Jin et al. [45] and Park et al. [46]

	SiC fibre	Pyrolytic carbon coating
Density ρ (kg/cm ³)	0.00237	0.0021
Shear modulus G (MPa)	83,480	10,710
Yield stress σ_y (MPa)	3400	590
Compressive modulus K (MPa)	91,430	50,000

Table 6 Parameters used for simulating single-grain scratching of SiC/SiC ceramics

Parameter	Description	Value	Unit
$a_{e,num}$	Simulation infeed	4; 8; 12; 16; 20	μm
a_p	SPH particle spacing of workpiece	2	μm
b_w	Workpiece width	0.288	mm
d_B	Thickness of carbon fibre coating	0.1–0.2	μm
d_F	SiC fibre diameter in the simulation model	10	μm
f	Volume fraction between matrix and fibre	0.4–0.5	–
h_w	Workpiece height	0.108	mm
l_w	Workpiece length	0.288	mm
$n_{p,EC}$	Number of SPH particles for one elementary cell	729	–
$n_{p,fm}$	Total number of SPH particles for the force model	1,119,744	–
$n_{p,sm}$	Total number of SPH particles for the surface model	1,020,600	–
$RMSE_{F_n}$	Averaged root-mean-square error of scratching normal force F_{ns}	5.27	N
v_c	Cutting speed	20	m/s
Δmesh	FE mesh size of diamond grain	2	μm
μ_d	Dynamic friction coefficient	0.26	–
μ_s	Static friction coefficient	0.6	–

The boundary conditions that fix the workpiece were chosen similarly to the WC-Co cemented carbide simulation model. Also, in this simulation, the contact between fibre, coating, and matrix did not have to be defined because both parts were modelled in SPH. A friction model was also used to model the contact between the diamond grain and workpiece material. Following Lyu et al., the static friction coefficient was set to $\mu_s = 0.6$ and the dynamic friction coefficient to $\mu_d = 0.26$ [47]. The parameters used for the simulation when single-grain scratching SiC/SiC ceramics are summarised in Table 6.

4 Simulation

The initial simulations of both models were validated with experimental results. In the following, the first simulation results of both models are compared to experimental data.

4.1 WC-Co cemented carbide

This section first explains the experimental setup of the WC-Co cemented carbide single-grain scratching experiments. Then, the simulation is validated.

4.1.1 Experimental setup

Data from already conducted single-grain scratching experiments with surface grinding kinematics was utilised to validate the simulation. The tool grinding machine ISOG S22P-Turbo from ISOG Technologies and the WC-Co cemented carbides listed in Table 1 were used for the experiments.

The experimental setup for the single-grain scratching tests is shown in Fig. 8.

The abrasive grains used were Element Six PDA657 7080 diamonds with an average grain diameter of $d_g = 213 \mu\text{m}$, which were electroplated onto a metal carrier and then bonded to a grain holder. The processes were carried out in the mode of up-grinding. The cutting speed was set to $v_c = 20 \text{ m/s}$, in accordance with grinding parameters commonly used in tool grinding. The diamond grains were scanned using a Keyence VK-X 150 confocal laser scanning microscope. The test points were replicated 15 times for statistical validation.

4.1.2 Validation

The engagement of the single-grain during simulating WC-Co cemented carbide scratching as a function of the simulation time t is shown in Fig. 9. After the diamond grain engagement with the workpiece started, the formation of a chip could be observed (Fig. 9 II). The WC-Co cemented carbide material was displaced to the lateral scratching track edges, forming a bulging. No chipping was observed at the scratching track edges. The shape of the scratch cross-sectional area corresponded in good approximation to the projection of the diamond grain geometry in a plane perpendicular to the scratch direction. In general, therefore, ductile chip formation can be assumed. This assumption corresponds to the explanatory model of chip formation according to Bifano [48] and Wirtz [49] for a chip thickness h_{cu} below the critical chip thickness $h_{cu,crit} = 9.32 \mu\text{m}$. The critical chip thickness is based on an empirical, analytical model. It calculates, as a function of material parameters, a critical infeed above which the machining behaviour changes from ductile to brittle-hard. The proportion of SPH particles displaced by the diamond grain, which were not discharged laterally but were trapped under the diamond grain, was dependent on the diamond grain geometry. No curvature of the formed chip in the scratching direction was visible. It can be assumed that this behaviour, which contradicts the actual process, is due to the non-application of the renormalization approximation. In LS-DYNA, the renormalization approximation offers the possibility of a more precise representation of the actual

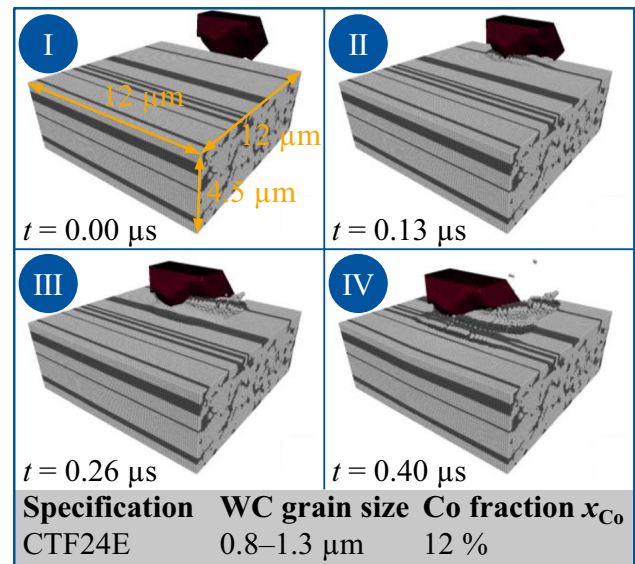


Fig. 9 Grain workpiece engagement during simulation

material removal behaviour by compensating missing neighbouring particles of near-edge particles using interpolation [19]. In the present model, the renormalization approximation would thus lead to an improved calculation in the contact zone between the workpiece and the diamond grain, as well as at the edges of the workpiece model and the formed chip. However, due to a sharp drop in the time step length in the simulation, the renormalization approximation could not yet be used. The influence of heat dissipation on chip formation was not simulated [50].

A central objective of the simulation is the prediction of scratching forces depending on the cemented carbide specification and the scratching process parameters. Therefore, the contact forces were recorded over the entire simulation runtime. Force characteristics were defined to compare the different simulations. In the normal and tangential directions, the mean value of the monitored force values was calculated over a specified period of time.

Figure 10 illustrates the influence of the cemented carbide specification on the simulated scratching forces. The infeed in the simulation was with $a_{e,s} = 1.5 \mu\text{m}$ much lower

Fig. 8 Experimental setup of the single-grain scratching experiments

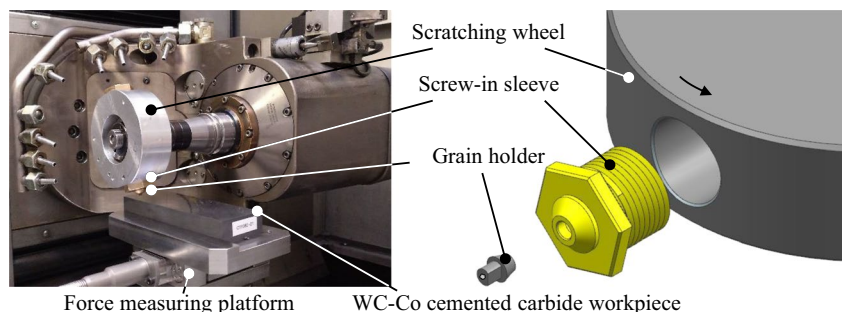
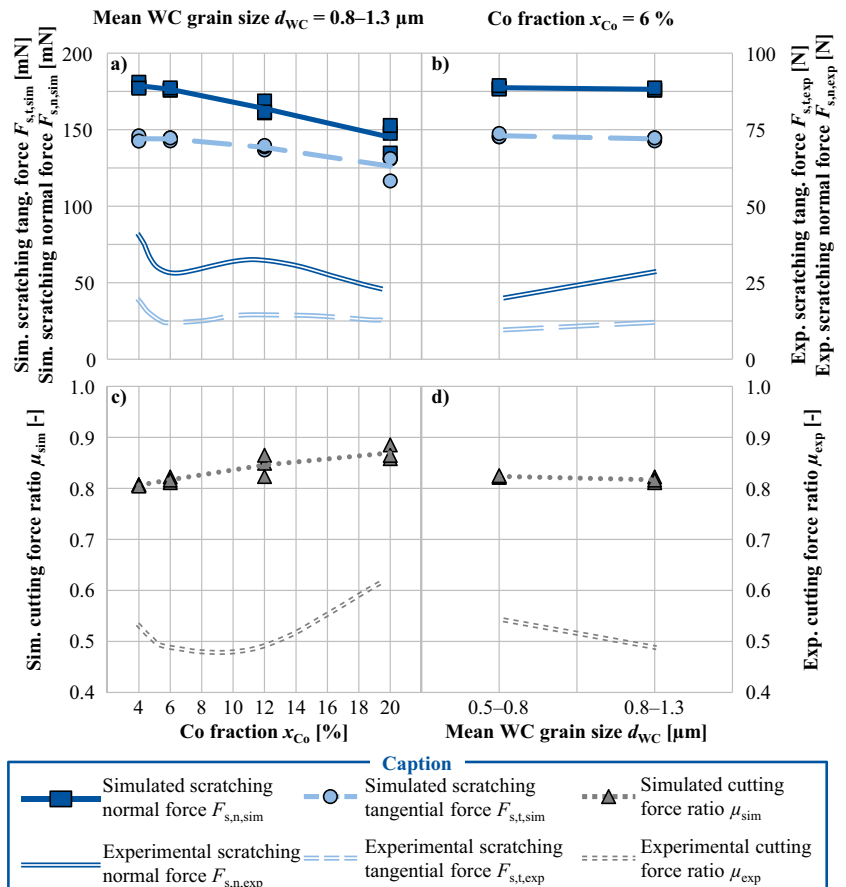


Fig. 10 Influence of the Co fraction and the mean WC grain size on the simulated scratching force and the cutting force ratio



compared to the empirical scratching experiments ($a_{e,e} = 20\text{--}30\ \mu\text{m}$) due to limited computation time, which is why the simulated scratching forces are lower than the experimental scratching forces. With further simulations, the model results will be fitted to the experimental results to enable the quantitative validation of the scratching forces. The simulated scratching forces decrease with increasing Co fraction and constant mean WC grain size (Fig. 10a). The observation can be explained by the fact that the material's overall strength decreases with increasing Co fraction, resulting in more ductile material behaviour. This phenomenon was also reflected in the empirical single-grain scratching experiments.

An increasing mean WC grain size at a constant Co fraction had an insignificant effect on the scratching forces in the simulation (Fig. 10b). In the empirical experiments, however, a drop in force was observed as the mean WC grain size decreased. Several reasons may be given for this discrepancy between experiment and simulation. On the one hand, only a very small volume element with a high particle spacing is considered in the simulation. Secondly, the simulation does not represent the grain boundaries between several WC grains. Accordingly, several WC grains that touch each other are assumed to be one grain. One big WC grain causes

higher forces during material removal than several small WC grains that are not connected. The smaller the average WC grain size, the more WC-WC grain boundaries exist in the real material structure. Smaller mean WC grain sizes thus led to lower forces in the experiments, whereas the union of several small WC grains led to comparably high forces in the simulation. Therefore, with larger average WC grain sizes, the scratching forces increased in the experiments, whereas the scratching forces remained constant in the simulation.

In addition to the scratching forces, the scratching force ratio μ , defined as the quotient of the scratching tangential force $F_{s,t}$ and the scratching normal force $F_{s,n}$, was evaluated. The cutting force ratio offers better comparability between simulation and experimental single-grain scratching investigations than the scratching forces since the influence of the lower infeed $a_{e,s}$ affected both the scratching tangential force $F_{s,t}$ and the scratching normal force $F_{s,n}$ and is thus less significant in the cutting force ratio. Due to strongly negative rake angles, the cutting force ratio in grinding is usually less than one [51]. The simulation correctly represented this principle (Fig. 10c, d). Figure 10c shows the influence of the Co fraction on the cutting force ratio. From the lowest to the highest cobalt fraction investigated, the simulated cutting force ratio μ increased by about $d = 7\%$. The empirical

experiments also showed that with increasing Co fraction, the cutting force ratio increases (Fig. 10c).

With an increasing WC grain size, the cutting force ratio slightly decreased in both the simulated and experimental results (Fig. 10d). Consequently, the qualitative trend of the cutting force ratio in the simulation was comparable to the empirical experiments. The fact that the cutting force ratios in the simulation are higher than in the experiments can be explained by the chip formation model of Martin [52]. The model states that a larger cutting force ratio compared to small cutting force ratios suggests more ductile material removal. In the simulation, the infeed $a_{e,s}$ was far below the transition to brittle-hard material removal $h_{cu,crit}$. In contrast, the infeed in the experiments $a_{e,e}$ was far above the limit. Accordingly, the more ductile machining in the simulation led to higher cutting force ratios.

In conclusion, the simulation could qualitatively reproduce the material removal behaviour. The empirical and numerical derived scratching and cutting force ratios largely followed the same trends. However, the simulation must be further developed at various approaches described above to predict values in the same order of magnitude.

4.2 SiC/SiC ceramics

This chapter presents the experimental setup of the single-grain scratching experiments of SiC/SiC ceramics and the validation.

4.2.1 Experimental setup

The empirical single-grain scratching experiments for validation were carried out on the ISOG S22P-Turbo tool grinding machine from ISOG Technologies. In Fig. 11, the test setup and the axis directions of the machine are shown. The grain holder with the diamond grain was screwed with the screw-in sleeve into the scratching wheel. The workpiece was mounted in a specially manufactured workpiece holder. A Kistler type 9119AA force measuring platform was mounted under the workpiece holder, continuously recording the scratching normal force $F_{n,s}$.

Several scratching tracks with increasing depths were placed next to each other in the scratching cone kinematics used for these experiments. Thus, the transition from ductile to brittle material removal behaviour could also be analysed. The scratching wheel rotated with a cutting speed of $v_c = 20$ m/s and moved with an axial feed in the y-direction and a radial feed in the x-direction. The resulting scratching tracks had a maximum depth of $a_{e,emp} = 20$ μ m. MBG-640 60/70 diamond grains from Diamond Innovations with an average grain diameter of $d_g = 213$ μ m were used. Blunt, pointed, and hybrid grains were used, respectively. SiC/SiC ceramics with dimensions of 30×30×.5 mm from the company BJS Composites GmbH were used. The fibre diameter of the Tyranno S SiC fibres from UBE Industries LTD was determined to $d_f = 10$ μ m by using scanning electron microscopy. Furthermore, the thickness of carbon fibre coating was $0.1 < d_b < 0.2$ μ m and the volume fraction between matrix and fibre was $0.4 < f < 0.5$. The test points were replicated three times for statistical validation.

4.2.2 Validation

For the validation of the simulated scratching normal force $F_{n,s}$ during single-grain scratching of SiC/SiC ceramics, the numerical and empirical interaction diagrams are compared in Fig. 12. In both interaction diagrams, the scratching normal force $F_{n,s}$ forms the scaling variable. Diagrams (a) and (b) show the influence of grain geometry and fibre orientation on the scratching normal force $F_{n,r}$. When comparing both diagrams, the same tendencies for the empirical and the numerical investigations are noticeable. One exception is the blunt grain, which, in contrast to the empirical tests, did not cause the highest scratching forces in the simulation. Concerning the fibre orientation, the transverse, longitudinal, 45-degree and normal orientation of the fibres were investigated. Diagrams (c) and (d) represent conditional changes in the scratching normal force $F_{n,s}$ caused by the variation of the grain geometry and the infeed. Diagrams (e) and (f) illustrate the correlation between fibre orientation, infeed, and the scratching normal force $F_{n,s}$ of the numerical and empirical investigations.

Fig. 11 Experimental setup of the single-grain scratching experiments

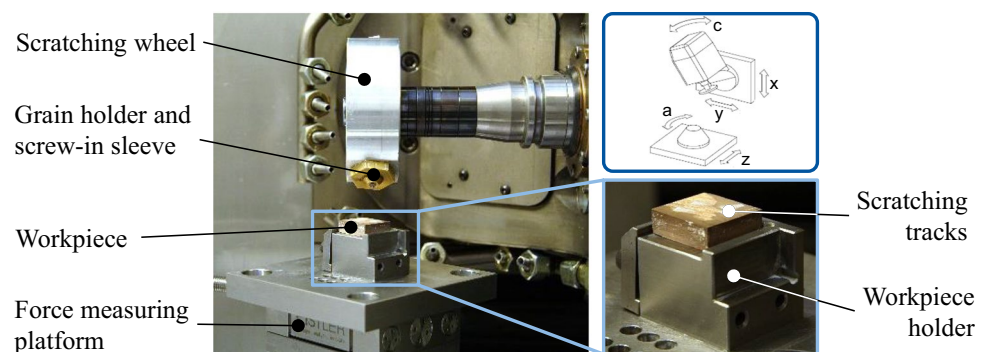
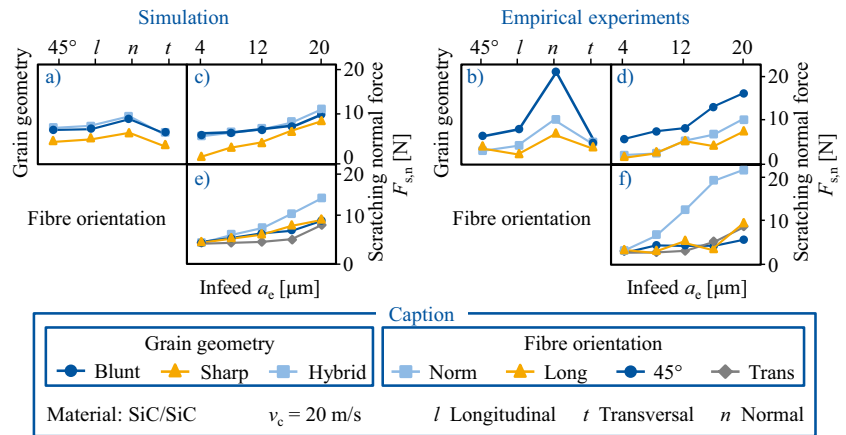


Fig. 12 Validation of the simulated scratching normal force based on interaction diagrams



At high infeed, the maximum values of the numerical scratching normal force $F_{n,s}$ were lower by a factor of 1.7 than those of the empirically determined scratching normal force $F_{n,s}$ (Fig. 12 c–f). Especially for infeed $a_c = 8 \mu\text{m}$ and higher, a significant difference between the graphs of the scratching normal force $F_{n,s}$ was identified. Incorrect development of the numerical model of the fibre-reinforced SiC/SiC non-oxide ceramics as the cause could be fundamentally ruled out since the curves of the scratching normal force $F_{n,s}$ of the sharp and hybrid grain geometries tended to coincide.

When comparing diagrams (e) and (f), the same tendencies between the numerical and empirical investigations were observed. Over the complete range of the varied infeed, the values of the monitored scratching normal forces of the 45-degree, longitudinal and transverse fibre orientation were in good agreement. Only the range of values of the normal fibre orientation showed a significant difference from the empirical experiments.

For the validation of the modelled scratching normal force $F_{n,s}$, it can be summarised that the developed

numerical simulation accurately represents the empirically determined scratching normal force. However, the blunt grain geometry should be compared again with the real grain geometry in further work since an unrepresentative grain geometry could cause the discrepancy between simulation and empirical tests. Therefore, only an averaged root-mean-square error of $RMSE_{Fns} = 5.27 \text{ N}$ was reached, which needs to be improved.

After both the empirical and numerical investigations, the scratching tracks were divided into two zones depending on the critical chip thickness. The zones differentiated between predominantly ductile and predominantly brittle machining. Within the zones, the documented surface phenomena, according to Müller, could be compared for the numerical and empirical tests [53]. Thus, it was possible to evaluate the ability of the numerical simulation to represent the material removal mechanisms correctly. Figure 13 compares the surface phenomena after the empirical tests with those generated in the simulation.

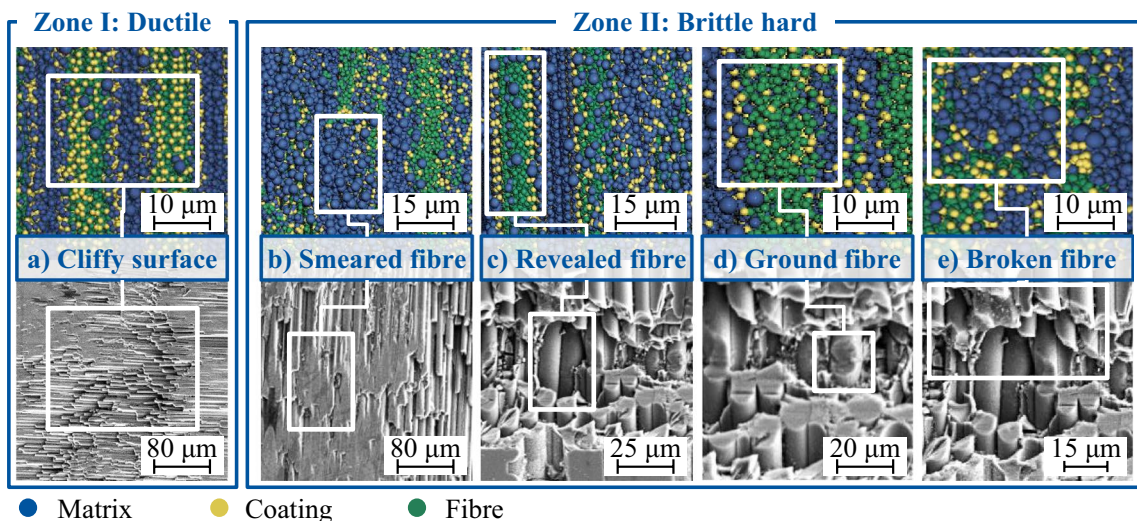


Fig. 13 Comparison of the surface phenomena of the numerical simulation and the empirical experiments

For the ductile material removal zone (zone I), the simulation could reproduce one of two surface phenomena recorded in the empirical experiments. The cliffy surface (Fig. 13a) could be identified in the ductile zone in the numerical and empirical tests. In the empirical tests, additional compressed particles appeared.

In the brittle material removal zone (zone II), four surface phenomena that occurred in the empirical tests could also be detected in the simulation. The detected surface phenomena are the smeared, revealed, ground, and broken fibre (Fig. 13b–e).

The matches of the modelled surface phenomena with the empirical experiments illustrate that a numerical SPH model's representation of the real single-grain scratching process is possible. However, characteristic surface phenomena, such as debonding and fibre pull-out, could not be recognised yet. It is to be assumed that the fixed particles at the edge of the workpiece inhibited the representation of further surface phenomena. For example, to image fibre pull-out, the ends of the fibre should not be subject to fixation. A more extensive and detailed model geometry of the fibre-reinforced SiC/SiC non-oxide ceramics could enable imaging of other surface phenomena in the simulation. However, the maximum modelling time of $t_{\text{solve,max}} = 24$ h required a compromise between the level of detail and the maximum model dimensions.

5 Conclusion and outlook

The study has shown that the material removal behaviour of two-phase brittle materials can be modelled by a combined simulation using SPH and FE methods. Two examples demonstrated this, the simulation of WC-Co cemented carbide and SiC/SiC non-oxide ceramics during single-grain scratching. Both simulations were validated with experimental data.

The simulation of WC-Co cemented carbide was first evaluated based on the optical material removal behaviour and compared with the experimental results. Subsequently, the forces were analysed. The simulation was able to qualitatively reproduce the scratching forces with sufficient accuracy. The cutting force ratio was used to minimise the effect of the low infeed in the simulation compared to the empirical experiments. The cutting force ratio was qualitatively in good approximation to the experimental results.

Further material parameters should be determined for the individual phases of the material to improve the simulation results quantitatively. Thus, a more complex material model could be used, such as Johnson-Holmquist-2 for the WC phase and Johnson-Cook for the Co phase. Furthermore, the application of the Massively Parallel-Processing version of LS-Dyna should be considered to be able to simulate higher infeed.

The simulation of SiC/SiC ceramics could also be validated using experimental data. The results were compared

with the help of an interaction diagram and corresponded in a good approximation to the experimental results. Only the blunt grain geometry showed discrepancies when compared to the experimental results. The simulation resulted in a more ductile material removal behaviour than the experiments. Furthermore, far-reaching similarities in the surface phenomena could be identified. The simulation of the SiC/SiC ceramics could also be optimised by determining separate material parameters for the individual material phases and, thus, by applying a more complex material model. The application of Massively Parallel-Processing in this simulation would allow the representation of additional surface phenomena observed in the experiments.

The hybrid simulation method led to a good compromise between computational time and simulation accuracy for both use cases. These results could not be achieved with pure FE simulations in preliminary work carried out by the authors because extensive computational time allowed only two-dimensional simulations which did not lead to accurate results. Furthermore, no simulation in the state of the art suits this use case. However, the models must be further developed to improve the prediction accuracies and shorten the computation times. Only then can the simulation truly substitute the extensive single-grain scratching experiments.

Author contributions All authors contributed to the study conception and design. The experiments and simulations were performed by Alexander Dehmer, Sebastian Prinz, and Peter Breuer. The first draft of the manuscript was written by Alexander Dehmer, and all authors commented on previous versions of the manuscript. All authors read and approved the final manuscript.

Funding Open Access funding enabled and organized by Projekt DEAL. This work was supported by the German Research Foundation (DFG) under Grant BE 2542/7-1 “Zerspanungstheorie beim Schleifen faserverstärkter N ichtoxidkeramiken” and Grant BE 2542/24-1 “Smooth Particle Hydrodynamic (SPH) Modeling of Grinding the SiC-SiC Ceramic Matrix Composite.” Simulations were performed with computing resources granted by RWTH Aachen University under project thes1047.

Declarations

Competing interests The authors declare no competing interests.

Open Access This article is licensed under a Creative Commons Attribution 4.0 International License, which permits use, sharing, adaptation, distribution and reproduction in any medium or format, as long as you give appropriate credit to the original author(s) and the source, provide a link to the Creative Commons licence, and indicate if changes were made. The images or other third party material in this article are included in the article's Creative Commons licence, unless indicated otherwise in a credit line to the material. If material is not included in the article's Creative Commons licence and your intended use is not permitted by statutory regulation or exceeds the permitted use, you will need to obtain permission directly from the copyright holder. To view a copy of this licence, visit <http://creativecommons.org/licenses/by/4.0/>.

References

- South J, Blass B (2001) *The future of modern genomics*. Blackwell, London
- Spur G, Niewelt W, Mei A (1995) Schleifen von Superlegierungen für Gasturbinen. *ZwF* 90:311–314. <https://doi.org/10.1515/zwf-1995-900618>
- Klocke F (2009) *Manufacturing processes 2: grinding, honing, lapping*. RWTHedition. Springer-Verlag Berlin Heidelberg, Berlin, Heidelberg. <https://doi.org/10.1007/978-3-540-92259-9>
- Denkena B, Köhler J, Schindler A (2014) Behavior of the magnetic abrasive tool for cutting edge preparation of cemented carbide end mills. *Prod Eng* 8:627–633. <https://doi.org/10.1007/s11740-014-0569-4>
- Denkena B, Friemuth T, Spengler C (2003) Modeling and process design for different grinding operations of carbide tools. *Prod Eng* 10:15–18
- König W, Steffens K, Ludewig T (1985) Single grit tests to reveal the fundamental mechanism in grinding. *Proc Grind Conf ASME* 16:141–154
- Wang B, Zhang Z, Chang K et al (2018) New deformation-induced nanostructure in silicon. *Nano Lett* 18:4611–4617. <https://doi.org/10.1021/acs.nanolett.8b01910>
- Zhang Z, Wang B, Kang R et al (2015) Changes in surface layer of silicon wafers from diamond scratching. *CIRP Annals* 64:349–352. <https://doi.org/10.1016/j.cirp.2015.04.005>
- Zhang Z, Wang X, Meng F et al (2022) Origin and evolution of a crack in silicon induced by a single grain grinding. *J Manuf Proc* 75:617–626. <https://doi.org/10.1016/j.jmapro.2022.01.037>
- Mackerle J (1999) Finite-element analysis and simulation of machining: a bibliography (1976–1996). *J Mater Process Technol* 86:17–44. [https://doi.org/10.1016/S0924-0136\(98\)00227-1](https://doi.org/10.1016/S0924-0136(98)00227-1)
- Setti D, Kirsch B, Aurich JC (2019) Experimental investigations and kinematic simulation of single grit scratched surfaces considering pile-up behaviour: grinding perspective. *Int J Adv Manuf Technol* 103:471–485. <https://doi.org/10.1007/s00170-019-03522-7>
- Lucy LB (1977) A numerical approach to the testing of the fission hypothesis. *Astronom J* 82:1013. <https://doi.org/10.1086/112164>
- Gingold RA, Monaghan JJ (1977) Smoothed particle hydrodynamics: theory and application to non-spherical stars. *Monthly Notices Royal Astronom Soc* 181:375–389. <https://doi.org/10.1093/mnras/181.3.375>
- Libersky LD, Petschek AG (1991) Smooth particle hydrodynamics with strength of materials. In: Trease HE, Fritts MF, Crowley WP (eds) *Advances in the Free-Lagrange Method Including Contributions on Adaptive Gridding and the Smooth Particle Hydrodynamics Method: Proceedings of the Next Free-Lagrange Conference Held at Jackson Lake Lodge, Moran, WY, USA 3-7 June 1990*. Springer, Berlin, Heidelberg, pp 248–257. <https://doi.org/10.1007/3-540-54960-9>
- Fraga Filho CAD (2019) *Smoothed particle hydrodynamics: fundamentals and basic applications in continuum mechanics*, 1st edn. Springer International Publishing, Cham
- Dirac PAM (1958) *The principles of quantum mechanics*. In: *The international series of monographs on physics*, 4th edn. Clarendon Pr, Oxford
- Monaghan JJ (2005) Smoothed particle hydrodynamics. *Rep Prog Phys* 68:1703–1759. <https://doi.org/10.1088/0034-4885/68/8/R01>
- Livermore Software Technology Corp (2019) *LS-Dyna Theory Manual: Draft Version*. Livermore, CA, USA
- Umer U, Mohammed MK, Qudeiri JA et al (2016) Assessment of finite element and smoothed particles hydrodynamics methods for modeling serrated chip formation in hardened steel. *Adv Mech Eng* 8. <https://doi.org/10.1177/1687814016652372>
- Limido J, Espinosa C, Salaün M et al (2007) SPH method applied to high speed cutting modelling. *Int J Mech Sci* 49:898–908. <https://doi.org/10.1016/j.ijmecsci.2006.11.005>
- Deng B, Yang M, Zhou L et al (2019) Smoothed particle hydrodynamics (SPH) simulation and experimental investigation on the diamond fly-cutting milling of zirconia ceramics. *Procedia CIRP* 82:202–207. <https://doi.org/10.1016/j.procir.2019.04.001>
- Zahedi SA, Demiral M, Roy A et al (2013) FE/SPH modelling of orthogonal micro-machining of f.c.c. single crystal. *Comput Mater Sci* 78:104–109. <https://doi.org/10.1016/j.commatsci.2013.05.022>
- Geng X, Dou W, Deng J et al (2017) Simulation of the cutting sequence of AISI 316L steel based on the smoothed particle hydrodynamics method. *Int J Adv Manuf Technol* 89:643–650. <https://doi.org/10.1007/s00170-016-9116-0>
- Heisel U, Zaloga W, Krivoruchko D et al (2013) Modelling of orthogonal cutting processes with the method of smoothed particle hydrodynamics. *Prod Eng* 7:639–645. <https://doi.org/10.1007/s11740-013-0484-0>
- Rüttimann N, Roethlin M, Buhl S et al (2013) Simulation of hexa-octahedral diamond grain cutting tests using the SPH method. *Procedia CIRP* 8:322–327. <https://doi.org/10.1016/j.procir.2013.06.110>
- Johnson GR, Holmquist TJ (1999) Response of boron carbide subjected to large strains, high strain rates, and high pressures. *J Appl Phys* 85:8060–8073. <https://doi.org/10.1063/1.370643>
- Niu W, Mo R, Liu GR et al (2018) Modeling of orthogonal cutting process of A2024-T351 with an improved SPH method. *Int J Adv Manuf Technol* 95:905–919. <https://doi.org/10.1007/s00170-017-1253-6>
- Wang J, Shimada K, Mizutani M et al (2018) Tool wear mechanism and its relation to material removal in ultrasonic machining. *Wear* 394–395:96–108. <https://doi.org/10.1016/j.wear.2017.10.010>
- Abena A, Essa K (2019) 3D micro-mechanical modelling of orthogonal cutting of UD-CFRP using smoothed particle hydrodynamics and finite element methods. *Compos Struct* 218:174–192. <https://doi.org/10.1016/j.compstruct.2019.03.037>
- Sridhar P, de Payrebrune KM (2019) Discretization approaches to model metal cutting with Lagrangian, arbitrary Lagrangian Eulerian and smooth particle hydrodynamics formulations. *Proc Appl Math Mech* 19. <https://doi.org/10.1002/pamm.201900413>
- Li BZ, Ni JM, Zhou ZX et al (2011) FEM simulation of strain rate in high speed grinding. *AMR* 223:813–820. <https://doi.org/10.4028/www.scientific.net/AMR.223.813>
- Kurlov AS, Gusev AI (2013) *Tungsten carbides: structure, properties and application in hardmetals*, vol 184, 4th edn. Springer International Publishing, Cham
- Csanádi T, Bfanda M, Duszová A et al (2014) Deformation characteristics of WC micropillars. *J Eur Ceram Soc* 34:4099–4103. <https://doi.org/10.1016/j.jeurceramsoc.2014.05.045>
- Özden UA (2015) *Finite element simulation of fatigue crack growth in hardmetal*. Dissertation, RWTH Aachen
- Kurzweil P (2020) *Chemie: Grundlagen, technische Anwendungen, Rohstoffe, Analytik und Experimente*, 11th edn. Springer Vieweg, Wiesbaden
- Chatti S, Laperrière L, Reinhart G et al (2019) *CIRP Encyclopedia of Production Engineering*, 2nd edn. Springer, Berlin Heidelberg, Berlin, Heidelberg
- Jianxin D, Hui Z, Ze W et al (2012) Friction and wear behaviors of WC/Co cemented carbide tool materials with different WC grain sizes at temperatures up to 600°C. *Int J Refract Met Hard Mater* 31:196–204. <https://doi.org/10.1016/j.ijrmhm.2011.11.003>

38. An Q, Chen J, Ming W et al (2021) Machining of SiC ceramic matrix composites: a review. *Chin J Aeronaut* 34:540–567. <https://doi.org/10.1016/j.cja.2020.08.001>
39. Chamberlain A, Lane J (2012) SiC/SiC ceramic matrix composites: a turbine engine perspective. In: Fahrenholtz W, Lee W, Wuchina EJ et al (eds) *Ultra-High Temperature Ceramics: Materials for Extreme Environmental Applications II Proceedings*
40. Murthy PL, Nemeth NN, Brewer DN et al (2008) Probabilistic analysis of a SiC/SiC ceramic matrix composite turbine vane. *Composites, Part B* 39:694–703. <https://doi.org/10.1016/j.compositesb.2007.05.006>
41. Brennan J (2000) Interfacial characterization of a slurry-cast melt-infiltrated SiC/SiC ceramic-matrix composite. *Acta Mater* 48:4619–4628. [https://doi.org/10.1016/S1359-6454\(00\)00248-2](https://doi.org/10.1016/S1359-6454(00)00248-2)
42. Riccardi B, Giancarli L, Hasegawa A et al (2004) Issues and advances in SiCf/SiC composites development for fusion reactors. *J Nucl Mater* 329–333:56–65. <https://doi.org/10.1016/j.jnucmat.2004.04.002>
43. Liang Z, Tian M, Wang Q et al (2018) Effect of single grit impacts on initiation and propagation of cracks in ultrasonic assisted grinding of ceramics by using SPH method. *Int J Nanomanuf* 14:387. <https://doi.org/10.1504/IJNM.2018.095326>
44. Cronin SD, Bui K, Kaufmann C et al (2003) Implementation and validation of the Johnson-Holmquist ceramic material model in LS-Dyna. In: *Proceedings of the 4th European LS-DYNA Users Conference*, pp 47–60
45. Jin E, Sun W, Liu H et al (2020) Effect of interface coating on high temperature mechanical properties of SiC–SiC composite using domestic Hi–Nicalon type SiC fibers. *Coatings* 10:477. <https://doi.org/10.3390/coatings10050477>
46. Park J (2009) *Bioceramics*. Springer, New York, New York, NY
47. Lyu Y, Tang H, Wang P (2019) Tribological properties of carbon fiber toughened SiC prepared by hot pressing sintering. *Ceram Int* 45:832–838. <https://doi.org/10.1016/J.CERAMINT.2018.09.250>
48. Bifano TG, Dow TA, Scattergood RO (1991) Ductile-regime grinding: a new technology for machining brittle materials. *J Eng for Industry* 113:184. <https://doi.org/10.1115/1.2899676>
49. Wirtz C (2018) *Zerspanverhalten von WC-Co Hartmetallen bei der Schleifbearbeitung*. Dissertation, RWTH Aachen
50. Klocke F (2018) *Fertigungsverfahren 1: Zerspanung mit geometrisch bestimmter Schneide*, vol 1, 9th edn. Springer Vieweg, Berlin
51. Huang S, Yu X (2018) A study of grinding forces of SiCp/Al composites. *Int J Adv Manuf Technol* 94:3633–3639. <https://doi.org/10.1007/s00170-017-1115-2>
52. Giwerzew A (2003) *Spanbildungsmechanismen und tribologisches Prozeßverhalten beim Schleifen mit niedrigen Schnittgeschwindigkeiten* (Dissertation). Universität Bremen
53. Müller S (2018) *Material removal mechanisms during grinding of fiber-reinforced ceramics with porous matrix*. Dissertation, RWTH Aachen

Publisher's note Springer Nature remains neutral with regard to jurisdictional claims in published maps and institutional affiliations.